RESEARCH ARTICLE

Structures, biomimetic synthesis, and anti-SARS-CoV-2 activity of two pairs of enantiomeric phenylpropanoid-conjugated protoberberine alkaloids from the rhizomes of *Corydalis decumbens*

Jing-Guang Lu[1] · Yingwei Wang[1] · Ming-Rong Yang[1] · Cai-Yun Wang[1] · Jieru Meng[1] ·
Jiazheng Liu[1] · Zifeng Yang[2] · Kongsong Wu[3] · Li-Ping Bai[1] · Guo-Yuan Zhu[1] ·
Zhi-Hong Jiang[1]

Abstract (±)-Decumicorine A (**1**) and (±)-*epi*-decumicorine A (**2**), two pairs of enantiomeric isoquinoline alkaloids featuring a novel phenylpropanoid-conjugated protoberberine skeleton, were isolated and purified from the rhizomes of *Corydalis decumbens*. The separation of (±)-**1** and (±)-**2** was achieved by chiral HPLC to produce four optically pure enantiomers. The structures and absolute configurations of compounds (−)-**1**, (+)-**1**, (−)-**2**, and (+)-**2** were elucidated by spectroscopic analysis, ECD calculations, and X-ray crystallographic analyses. The two racemates were generated from a Diels-Alder [4 + 2] cycloaddition between jatrorrhizine and ferulic acid in the proposed biosynthetic pathways, which were fully verified by a biomimetic synthesis. Moreover, compound (+)-**1** exhibited an antiviral entry effect on SARS-CoV-2 pseudovirus by blocking spike binding to the ACE2 receptor on HEK-293T-ACE2^h host cells.

✉ Li-Ping Bai
lpbai@must.edu.mo

✉ Guo-Yuan Zhu
gyzhu@must.edu.mo

✉ Zhi-Hong Jiang
zhjiang@must.edu.mo

[1] State Key Laboratory of Quality Research in Chinese Medicine, Guangdong-Hong Kong-Macao Joint Laboratory of Respiratory Infectious Disease, Macau Institute for Applied Research in Medicine and Health, Macau University of Science and Technology, Macau 999078, People's Republic of China

[2] State Key Laboratory of Respiratory Disease, National Clinical Research Center for Respiratory Disease, Guangzhou Institute of Respiratory Health, The First Affiliated Hospital of Guangzhou Medical University, Guangzhou 510120, People's Republic of China

[3] Jiangxi Kangenbei Tianshikang Chinese Traditional Medicine Co. Ltd, Jiangxi 335200, People's Republic of China

Introduction

Decumbent Corydalis Rhizome (DCR) is the dried tuber of *Corydalis decumbens* (Thunb.) Pers. ("Xia-tian-wu" in Chinese) from the Papaveraceae family. *Flora of China* states that the geographical distribution of *C. decumbens* mainly includes the Chinese provinces of Jiangxi, Jiangsu, Zhejiang, Anhui, Fujian, Hubei, Hunan, Shanxi, and Southern Japan. According to the latest *Chinese Pharmacopoeia* (ChP 2020), DCR and the therapeutic drugs, which were developed from its total alkaloids in various dosage forms (tablets, eye drops, and so on), are clinically used in China for treating hemiplegia caused by wind-stroke, headache, traumatic injuries, and other painful diseases. Isoquinoline alkaloids are well known, rich in species from the genus *Corydalis* and are considered principal bioactive constituents (Iranshahy et al. 2014; Deng et al. 2021). At present, more than 70 isoquinoline alkaloids (which are summarized at https://www.nmrdata.com) have been isolated from DCR, including the typical isoquinoline alkaloids palmatine, berberine, and *l*-tetrahydropalmatine. The objective of this research was to discover more isoquinoline alkaloids in DCR that are structurally unique and biologically active. In this study, LC–MS analysis indicated that obvious alkaloids were still observed

in the aqueous layer of total alkaloids after adequate partitioning was achieved. Finally, (±)-decumicorine A (**1**) and (±)-*epi*-decumicorine A (**2**), two pairs of enantiomeric isoquinoline alkaloids that contain a novel carbon framework of phenylpropanoid-conjugated protoberberine, were obtained (Fig. 1) (Tantillo 2021) from the aqueous layer of total alkaloids after partitioning with the organic solvent. Herein, we report the isolation, structural determination, plausible biosynthetic pathways, biomimetic synthesis, and anti-SARS-CoV-2 activity of these compounds.
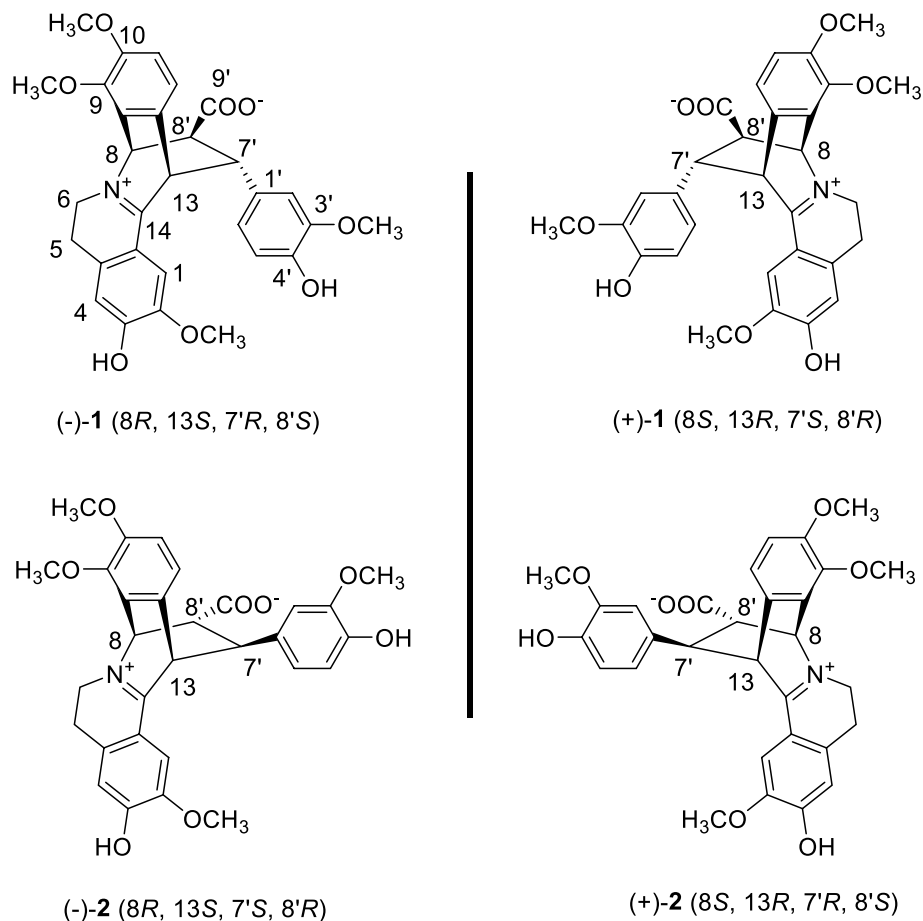
Materials and methods

General experimental procedures

Optical rotations were performed on a Rudolph Research Autopol I automatic polarimeter (Rudolph Research Analytical, NJ, USA). UV and CD spectra were measured on a JASCO High performance J-1500 CD spectrometer (JASCO, Tokyo, Japan). IR spectra were recorded on an Agilent Cary 600 series FT-IR spectrometer (KBr) (Agilent Technologies, CA, USA). The melting point was obtained on a BA-350 melting point apparatus (BenAng, Shanghai, China). 1D

and 2D NMR spectra were acquired on a Bruker Ascend™ 600 MHz NMR spectrometer (Bruker, Fällanden, Switzerland). LC-MS and HR-ESI-MS spectra were determined using an Agilent 1290 Infinity II UHPLC combined with a 6230 high-resolution TOF-MS system with an Agilent Poroshell 120 EC-C_{18} column (2.7 μm, 100×4.6 mm, i.d.) (Agilent Technologies, CA, USA). Semipreparative HPLC was carried out on an Agilent 1200 series HPLC system (Agilent Technologies, CA, USA) using Waters Xselect CSH Phenyl-Hexyl (5 μm, 250×10 mm, i.d.) column (Waters, MA, USA) with a constant flow of 3.0 mL/min. Preparative-HPLC was conducted on an LabAlliance HPLC system (LabAlliance, NY, USA) using Grace VisionHT C_{18} (5 μm, 250×22 mm, i.d.) column (Grace Davision Discovery Sciences, Lokeren, Belgium) under an isocratic flow of 15.0 mL/min. MPLC was performed on a Büchi Sepacore flash chromatography system (Büchi, Flawil, Switzerland) using a self-prepared C_{18} column (Unisil 10–120 μm C_{18} Ultra Plus, 460×36 mm, i.d., Suzhou NanoMicro Technology Co., Ltd., China) with a gradient eluted program. The above-utilized mobile phases were composed of MeCN and H_2O containing either 0.1% formic acid (FA), or 10 mM ammonium acetate (AA), or a buffer of 0.1% FA and 10 mM AA. Column chromatography (CC) was performed with a

Fig. 1 Structures of compounds **1** and **2**

(-)-**1** (8*R*, 13*S*, 7'*R*, 8'*S*)

(+)-**1** (8*S*, 13*R*, 7'*S*, 8'*R*)

(-)-**2** (8*R*, 13*S*, 7'*S*, 8'*R*)

(+)-**2** (8*S*, 13*R*, 7'*R*, 8'*S*)

microporous adsorbent resin (D101, Sinopharm Chemical Reagent Co., Ltd, Shanghai, China; 2.8 L, 610×76 mm, i.d.) as packing material. Chiral-LC separation was carried out on a CHIRALCEL® OZ-H chiral column (5 μm, 250×10 mm, i.d.) (Chiral Technologies, PA, USA), with a mobile phase of *n*-hexane and absolute EtOH containing a buffer of 0.1% glacial acetic acid (GAA) and 0.1% diethyl ammonium (DEA), under an isocratic flow of 3.0 mL/min. Reference compounds of jatrorrhizine hydrochloride and ferulic acid were purchased from Chengdu MUST Bio-Technology Co., Ltd (Chengdu, China). All solvents and reagents were in either spectroscopic, or HPLC, or ACS grade.

Plant materials

The rhizomes of *Corydalis decumbens* (Decumbent Corydalis Rhizome, DCR) were collected in May 2018 from the culture field of Jiangxi HERBISKY Chinese Medicine Co., Ltd., Jiangxi Province, China, and were authenticated by the author, Prof. Zhi-Hong Jiang. The voucher specimen (DCR-2018-05) was deposited at the State Key Laboratory of Quality Research in Chinese Medicine, Macau University of Science and Technology.

Extraction and isolation

The air-dried DCR (6 kg) was powdered and extracted with 80% EtOH (24 L × 3) under reflux. The extracted solutions were concentrated under reduced pressure to obtain a total extract, which was subsequently dissolved in 1% HCl (8 L) and centrifuged under 3500 rpm for 30 min to remove non-alkaloid fraction (Zhu et al. 2014). The supernatant was adjusted to pH 10.0 with ammonia water to precipitate alkaloids, and then partitioned by CH_2Cl_2 and water-saturated *n*-BuOH, successively. The aqueous layer (W, 762 g) was subjected to the D101 resin CC eluting with H_2O, 10%, 20%, and 95% EtOH (each 8 L) successively to afford the corresponding fractions W-a–W-d. After removal of the solvent, fraction W-d (20 g) was isolated by MPLC system using gradient program of MeCN–H_2O (10:90 → 60:40, v/v, H_2O containing 10 mM AA) to afford 9 fractions (W-d-1–W-d-9). W-d-4 (2.3 g) was further isolated with preparative HPLC and eluted with MeCN–H_2O (23:77, v/v, H_2O containing 0.1% FA and 10 mM AA) to obtain 4 subfractions (W-d-4-1–W-d-4-4). W-d-4-2 (610 mg) was separated and purified by semipreparative HPLC with MeCN–H_2O (22:78, v/v, H_2O containing 0.1% FA) to afford compound **1** (58 mg, t_R = 10.0 min). In a similar manner, W-d-6 (2.0 g) was finally isolated and purified by semipreparative HPLC with MeCN–H_2O (23:77, v/v, H_2O containing 0.1% FA) to afford compound **2** (180 mg, t_R = 13.5 min). Compound **1** (11.7 mg) was further separated by chiral HPLC and eluted with *n*-hexane–EtOH (65:35, v/v, containing 0.1% GAA and

0.1% DEA) to afford (-)-**1** (t_R 41.2 min, 5.3 mg) and (+)-**1** (t_R 51.9 min, 5.6 mg). Compound **2** (22 mg) was further isolated by chiral HPLC and eluted with *n*-hexane–EtOH (55:45, v/v, containing 0.1% GAA and 0.1% DEA) to obtain (−)-**2** (t_R 19.3 min, 10.2 mg) and (+)-**2** (t_R 27.8 min, 10.0 mg). Compounds (−)-**1**, (+)-**1**, (−)-**2** and (+)-**2** were finally purified with the same semipreparative HPLC conditions mentioned above to remove the remaining salt derived from GAA and DEA.

(±)-Decumicorine A (**1**): yellowish brown crystal (MeOH/H_2O, 5:1, v/v); m.p. 177–178 °C; $[\alpha]^{20}_D$ 1.7 (*c* 0.5, MeOH); UV (MeOH) λ_{max} (log ε) 232.0 (4.04), 255.3 (3.84), 276.0 (3.78), 317.0 (3.52) nm; IR (KBr) ν_{max} 3564, 3389, 3019, 2964, 2937, 2837, 1614, 1574, 1516, 1493, 1402, 1325, 1302, 1261, 1215, 1163, 1134, 1078, 1003, 964, 874, 849 cm^{-1}. ^1H and ^{13}C NMR data, see Table 1; HRMS (ESI-TOF) *m/z* 532.1945 [M + H]$^+$ (calcd. for $C_{30}H_{29}NO_8$, 532.1966); (−)-**1**: light yellow crystal (MeOH/H_2O, 5:1, v/v); m.p. 164–165 °C; $[\alpha]^{20}_D$ -110.4 (*c* 0.5, MeOH); ECD (MeOH) λ_{max} ($\Delta\varepsilon$) 207.1 (− 20.2), 234.5 (5.5), 251.5 (− 2.7), 278.2 (− 3.0) nm. (+)-**1**: yellowish brown crystal (MeOH/H_2O, 5:1, v/v); m.p. 171–172 °C; $[\alpha]^{20}_D$ 118.1 (*c* 0.5, MeOH); ECD (MeOH) λ_{max} ($\Delta\varepsilon$) 206.5 (21.1), 233.0 (− 5.1), 251.8 (3.1), 275.5 (2.9) nm.

(±)-*Epi*-decumicorine A (**2**): light-yellow crystal (absolute EtOH/H_2O, 30:1, v/v); m.p. 187–188 °C; $[\alpha]^{20}_D$ 2.2 (*c* 0.5, MeOH); UV (MeOH) λ_{max} (log ε) 252.1 (4.11), 276.0 (3.80), 313.9 (3.93), 375.9 (4.06) nm; IR (KBr) ν_{max} 2999, 2941, 2835, 1717, 1670, 1609, 1556, 1518, 1493, 1464, 1431, 1398, 1373, 1313, 1273, 1227, 1161, 1080, 1001, 851, 804 cm^{-1}. ^1H and ^{13}C NMR data, see Table 1; HRMS (ESI-TOF) *m/z* 532.1979 [M + H]$^+$ (calcd. for $C_{30}H_{29}NO_8$, 532.1966); (−)-**2**: light yellow powder; $[\alpha]^{20}_D$ − 139.1 (*c* 0.5, MeOH); ECD (MeOH) λ_{max} ($\Delta\varepsilon$) 203.5 (− 23.8), 231.1 (6.0), 247.8 (− 2.2) nm. (+)-**2**: light yellow powder; $[\alpha]^{20}_D$ 148.4 (*c* 0.5, MeOH); ECD (MeOH) λ_{max} ($\Delta\varepsilon$) 203.5 (26.7), 230.5 (− 7.1), 247.2 (2.8) nm.

ECD calculations

In general, conformational analyses were carried out *via* random searching in the Sybyl-X 2.0 (Tripos Associates Inc., St. Louis, MO, USA) using the MMFF94S force field with an energy cutoff of 2.5 kcal/mol. The results showed ten lowest energy conformers for both compounds. Subsequently, the conformers were re-optimized using DFT at the PBE0-D3(BJ)/def2-SVP level in MeOH using the polarizable conductor calculation model (SMD) by the ORCA4.2.1 program (Neese 2012, 2018). The energies, oscillator strengths, and rotational strengths (velocity) of the first 30 electronic excitations were calculated using the TDDFT methodology at the PBE0-D3(BJ)/def2-TZVP level in MeOH. The ECD spectra were simulated by the overlapping Gaussian function

Table 1 NMR spectroscopic data for **1** and **2** in CD$_3$OD[#]

Position	**1**		**2**	
	δ_H(J, Hz)	δ_C	δ_H(J, Hz)	δ_C
1	6.83, s	113.1	7.69, s	113.5
1a		115.8		115.3
2		149.9		149.4
3		162.0		158.9
4	6.69, s	117.4	6.86, s	117.2
4a		135.1		135.8
5	3.10, m; 3.03, m	27.2	3.31, overlap; 2.98, dt (16.8, 6.0)	26.8
6	4.40, m; 4.15, m	49.5	4.32, m; 4.04, m	51.0
8	6.00, d (3.6)	64.7	6.03, d (1.2)	64.8
8a		129.1		131.5
9		146.4		145.1
10		153.6		153.9
11	7.01, d (8.1)	113.9	7.03, d (7.8)	113.8
12	7.29, d (8.1)	120.9	7.05, d (7.8)	124.3
12a		130.6		127.2
13	5.27, d (2.4)	51.2	5.21, d (2.4)	50.0
14		176.5		176.6
1′		133.1		132.4
2′	6.66, d (1.8)	112.6	5.88, d (1.8)	112.3
3′		149.1		148.6
4′		147.0		147.1
5′	6.64, d (8.1)	116.4	6.61, d (8.4)	116.0
6′	6.62, dd (8.1, 1.8)	121.5	6.31, dd (8.4, 1.8)	122.4
7′	3.89, dd (6.0, 2.4)	49.4	3.65, dd (5.4, 2.4)	46.5
8′	3.53, dd (6.0, 3.6)	54.6	2.92, dd (5.4, 1.2)	56.0
9′		174.5		176.7
2-OCH$_3$	3.66, s	56.6	3.99, s	57.2
9-OCH$_3$	3.96, s	62.1	4.02, s	62.4
10-OCH$_3$	3.87, s	56.6	3.90, s	56.8
3′-OCH$_3$	3.63, s	56.3	3.56, s	55.6

[#]Data were assigned by the DEPT, HSQC, HMBC, ^{1}H–^{1}H COSY, and NOESY spectra.

(half the bandwidth at 1/e peak height, sigma = 0.30 for all) (Stephens and Harada 2010). To obtain the final spectra, the simulated spectra of the conformers were averaged according to the Boltzmann distribution theory and their relative Gibbs free energy (ΔG). By comparing the experiment spectra with the calculated model molecules, the absolute configuration of the only chiral center was finally determined.

X-ray crystallography

Crystal Data for **1** with C$_{30}$H$_{29}$NO$_8$ (M = 531.54 g/mol): monoclinic, space group P2$_1$/c (no. 14), a = 14.1060(2) Å, b = 13.1956(2) Å, c = 15.7116(2) Å, β = 100.3350(10)°,

V = 2877.06(7) Å^3, Z = 4, T = 150.00(10) K, μ(Cu Kα) = 0.740 mm^{-1}, $Dcalc$ = 1.227 g/cm^3, 27,805 reflections measured (6.37° ≤ 2Θ ≤ 147.004°), 5734 unique (R_{int} = 0.0416, R_{sigma} = 0.0235) which were used in all calculations. The final R_1 was 0.0491 (I > 2σ(I)) and wR_2 was 0.1359 (all data), Goodness-of-fit on F^2 = 1.041.

Crystal Data for (−)-**1** with C$_{30}$H$_{38}$NO$_{12.5}$ (C$_{30}$H$_{29}$NO$_8$·4.5H$_2$O, M = 612.61 g/mol): orthorhombic, space group P2$_1$2$_1$2$_1$ (no. 19), a = 12.8256(4) Å, b = 15.1527(3) Å, c = 30.4200(7) Å, V = 5950.9(3) Å^3, Z = 8, T = 149.99(10) K, μ(Cu Kα) = 0.900 mm^{-1}, $Dcalc$ = 1.368 g/cm^3, 20,280 reflections measured (5.81° ≤ 2Θ ≤ 147.336°), 11,274 unique (R_{int} = 0.0292, R_{sigma} = 0.0424) which were used in all calculations. The final R_1 was 0.1152 (I > 2σ(I)) and wR_2 was 0.3400 (all data), Goodness-of-fit on F^2 = 1.419, Flack/Hooft parameter = 0.03(9)/0.06(9).

Crystal Data for (+)-**1** with C$_{30}$H$_{36}$NO$_{12}$ (C$_{30}$H$_{29}$NO$_8$·4H$_2$O, M = 602.60 g/mol): orthorhombic, space group P2$_1$2$_1$2$_1$ (no. 19), a = 12.7247(2) Å, b = 15.0980(3) Å, c = 30.3866(5) Å, V = 5837.76(19) Å^3, Z = 8, T = 149.99(10) K, μ(Cu Kα) = 0.896 mm^{-1}, $Dcalc$ = 1.371 g/cm^3, 24,829 reflections measured (5.816° ≤ 2Θ ≤ 147.72°), 11,219 unique (R_{int} = 0.0223, R_{sigma} = 0.0294) which were used in all calculations. The final R_1 was 0.1249 (I > 2σ(I)) and wR_2 was 0.3664 (all data), Goodness-of-fit on F^2 = 1.611, Flack/Hooft parameter = 0.08(7)/0.11(6).

Crystal Data for **2** with C$_{30}$H$_{29}$NO$_8$·H$_2$O (M = 549.56 g/mol): monoclinic, space group I2/a (no. 15), a = 18.2529(7) Å, b = 9.8066(4) Å, c = 28.5267(11) Å, β = 91.824(4)°, V = 5103.7(3) Å^3, Z = 8, T = 100.0(3) K, μ(Cu Kα) = 0.882 mm^{-1}, $Dcalc$ = 1.430 g/cm^3, 16,816 reflections measured (6.2° ≤ 2Θ ≤ 147.502°), 5069 unique (R_{int} = 0.0863, R_{sigma} = 0.0645) which were used in all calculations. The final R_1 was 0.0682 (I > 2σ(I)) and wR_2 was 0.1935 (all data), Goodness-of-fit on F^2 = 1.079.

Compounds **1**, (−)-**1**, (+)-**1**, and **2** were separately collected at 150(10), 149.99(10), 149.99(10), and 100(3) K on a Rigaku Oxford Diffraction Supernova Dual Source, Cu at Zero equipped with an AtlasS2 CCD using Cu Kα radiation. The data were processed using CrysAlisPro (Oxford Diffraction Ltd., Abingdon, England, UK, 201024). The structures were solved by direct methods using Olex2 software (Dolomanov et al. 2009), and the non-hydrogen atoms were located from the trial structure and then refined anisotropically with SHELXL-2018 (Kratzert et al. 2015) using a full-matrix least squares procedure based on F^2. The weighted R factor, wR and goodness-of-fit S values were obtained based on F^2. The hydrogen atom positions were fixed geometrically at the calculated distances and allowed to ride on their parent atoms. Crystallographic data for the structures of **1**, (−)-**1**, (+)-**1**, and **2** reported in this paper have been deposited at the Cambridge Crystallographic Data Center and allocated with the deposition numbers: CCDC 2106787,

2106788, 2106791, and 2106792 for compounds **1**, (−)-**1**, (+)-**1**, and **2**, respectively. The ORTEP diagrams of (−)-**1**, (+)-**1**, and **2** described below are derived from their crystals without hydration.

Biomimetic synthesis

A mixture of jatrorrhizine hydrochloride (3.73 mg, 0.01 mmol) and excessive ferulic acid (3.88 mg, 0.02 mmol) was dissolved in 1 mL of anhydrous methanol, and then anhydrous potassium carbonate (2.76 mg, 0.02 mmol) was added to the above solution under temperature of 38 °C. The reaction was monitored by LC-MS for a complete conversion of jatrorrhizine hydrochloride (6 days). The reaction mixture was first neutralized by FA (1.5 μL, 0.04 mmol), and then was isolated by semipreparative HPLC using MeCN–H$_2$O (20 : 80, v/v, H$_2$O containing 0.1% FA) to give two compounds **syn-1** (1.07 mg) and **syn-2** (3.10 mg), of which MS spectra, ^{1}H/^{13}C NMR data, and chiral-HPLC chromatograms were identical to those of compounds **1** and **2** (see the supporting information for details). Other experimental conditions (Bradsher and Day 1971; Cavé et al. 1980; Gupta and Franck 1987; Mallamo et al. 1994) were also investigated as shown in Table 2.

Inhibition of entry of SARS-CoV-2 pseudovirus into HEK-293T-ACE2[h] cells (Guo et al. 2021; Zhang et al. 2021)

Firstly, the HEK-293T-ACE2[h] cells (Sino Biological, Beijing, China) were seeded in 96-well plates at 1×10^4 cells in 100 μL DMEM per well. The cells were cultured in a 37 °C incubator containing 5% CO$_2$ for 24 h. 30 μL of SARS-CoV-2 spike pseudovirus (Sino Biological, Beijing, China, PSV001) diluted in 70 μL of medium was mixed with 100 μL either compounds-containing or SARS-CoV-2 antibody-containing media. The above 200 μL of pseudovirus and compound (antibody) mixture solution was then immediately added into each well to infect cells for 2 h incubation in the 37 °C incubator. After the inoculum was disposed, cells were then overlaid with 100 μL fresh DMEM media, and incubated for 48 h at 37 °C with 5% CO$_2$. After that, the culture medium was removed and 100 μL of cell lysate was added into each well. After 10 min, the luciferase luminescence was measured at 568 nm by a microplate reader immediately after 100 μL of luminescence solution was added into each well according to the instruction from the Firefly Luciferase Reporter Gene Assay Kit (Beyotime, RG005). HEK293T/hACE2 cells infected only with SARS-CoV-2 pseudovirus were utilized as control group, and the luciferase luminescence value of the pseudovirus control group was defined as 100%, and the values of luminescence of either compound-treated or antibody-treated groups were normalized accordingly. Data were from three independent experiments.

Bio-layer interferometry (BLI)

The binding kinetics of the isolated compounds and ACE2 protein with the protein of SARS-CoV-2 spike RBD were analyzed by bio-layer interferometry on an Octet system (ForteBio, Octet RED96). A histidine-tagged SARS-CoV-2 spike RBD protein (25 μg/mL aqueous solution, Sino Biological, Cat 40592-V08H) was immobilized on a nickel charged nitrilotriacetic acid (Ni-NTA) biosensors (Fortebio, Inc) by a protein-loading program of the instrument. Each stock solution of samples (50 mM in DMSO) was serially diluted by PBS buffer with a final DMSO concentration of 0.2%. Protein-immobilized biosensors were equilibrated in PBS buffer for 10 min at room temperature before preceding data acquisition, and all experiments were performed at 30 °C. The Spike RBD-coated biosensors were dipped in wells containing serially diluted samples, along with ACE2 protein (positive control). The signal of background was subtracted from all samples by dipping a protein-immobilized biosensor in the blank buffer. The subtracted sensorgrams were then fitted to a 1:1 binding model by using Octet Data Analysis Software v11.1 (ForteBio) to calculate the equilibrium dissociation constant (K$_D$) values.

Molecular docking study

CDOCKER of Discovery Studio software was utilized to conduct molecular docking study on the structure of viral

Table 2 Experimental conditions studied for Diels-Alder [4 + 2] reaction

No.	Reaction conditions	Products and isolated yields
1	Anhydrous MeOH and K$_2$CO$_3$, 38 °C, 6 days	(±)-1 and (±)-2 (1 : 3), ~78.3% yield
2	Anhydrous MeOH and CaCO$_3$, N$_2$, 38–50 °C, 6 days	No reaction
3	Bromobenzene, 100 °C, 10–24 h	No reaction
4	ACN, hydroquinone, 5 days	No reaction
5	ACN, reflux heat, N$_2$, 16 h	No reaction

spike RBD from SARS-CoV-2 (PDB ID: 6M0J) with compound (+)-**1**. The active contact sites were determined to be GLN493, GLN498, TYR453, and SER494 of the spike RBD with ACE2 receptor according to the reported literature (Ding et al. 2020; Shang et al. 2020). The binding mode was analyzed with the Discovery Studio software.

Results

Structure elucidation

(±)-Decumicorine A (**1**) was obtained as a yellowish-brown crystal (MeOH/H$_2$O, 5:1, v/v; m.p. 177–178 °C). Its molecular formula was determined to be C$_{30}$H$_{29}$NO$_8$ by HR-ESI-TOF-MS analysis (*m/z* 532.1945 [M+H]$^+$, calcd 532.1966), revealing 17 unsaturated degrees in **1**. Analysis of the ^{1}H NMR data (Table 1) showed the presence of an ABX spin system at δ$_H$ 6.66 (d, *J* = 1.8 Hz, H-2′), 6.64 (d, *J* = 8.1 Hz, H-5′), and 6.62 (dd, *J* = 8.1, 1.8 Hz, H-6′), an AB spin system at δ$_H$ 7.01 (d, *J* = 8.1 Hz, H-11) and 7.29 (d, *J* = 8.1 Hz, H-12), two aromatic singlets at δ$_H$ 6.69 (s, H-4) and 6.83 (s, H-1), four methoxy groups (each s, δ$_H$ 3.66, 3.96, 3.87, and 3.63), two coupled methylenes at δ$_H$ 3.10 and 3.03 (both m, H$_2$-5), and δ$_H$ 4.40 and 4.15 (both m, H$_2$-6), and four continuously linked methines at δ$_H$ 6.00 (d, *J* = 3.6 Hz, H-8), 3.53 (dd, *J* = 6.0, 3.6 Hz, H-8′), 3.89 (dd, *J* = 6.0, 2.4 Hz, H-7′), and 5.27 (d, *J* = 2.4 Hz, H-13). Comprehensive interpretation of the ^{13}C NMR, DEPT, and HSQC spectra revealed four methoxy groups, two methylenes, four aliphatic methines, eighteen aromatic carbons (eleven aromatic non-protonated carbons), one carbonyl unit (δ$_C$ 174.5, C-9′), and one characteristic carbon (δ$_C$ 176.5, C-14) for the conjugated iminium nitrogen-carbon double bonds (Cavé et al. 1980) in **1**. According to the HR-TOF-MS and NMR data, compound **1**

has one trisubstituted benzene unit, two (*ortho-* and *para-*) tetrasubstituted benzene units, one carbonyl group, and one conjugated iminium nitrogen-carbon double bond. These functional groups occupied 14 degrees of unsaturation, indicating the presence of three additional cyclic groups in the skeleton of **1**. The ^{1}H–^{1}H COSY spectrum of **1** displayed homonuclear correlations for H-11/H-12, H-5′/H-6′, H$_2$-5/ H$_2$-6, and H-8/H-8′/H-7′/H-13, which corresponded to the aforementioned coupling peaks in its ^{1}H NMR spectrum, revealing that compound **1** contains four vicinal coupling fragments (Fig. 2, bold lines). The HMBC spectrum of **1** (Fig. 2) showed correlations from H$_2$-5 to C-1a/C-4, H-4 to C-1a/C-5, and H-1 to C-4a/C-14, indicating that C-5 is linked with C-4a, and C-14 is connected to C-1a. The HMBC correlations between H$_2$-6 and C-4a/C-8/C-14 as well as their chemical shift values indicated that the nitrogen atom was shared by three carbons, C-6/C-8/C-14, and formed a conjugated iminium nitrogen-carbon double bond with C-14, which produced an isoquinoline skeleton. A protoberberine skeleton fragment (Fig. 2 and **1F**) was deduced from the HMBC correlations from H-8 to C-6/C-9/C-12a/C-14, H-13 to C-1a/C-8a/C-12, and H-12 to C-8a/C13. C-7′ linked with C-1′ from the trisubstituted benzene ring was assigned based on the HMBC correlations between H-7′/H-8′/H-13 and C-1′ and between H-7′ and C-2′/C-6′. Considering the molecular formula of **1**, the HMBC correlation from H-7′/H-8′ to C-9′ indicated that C-8′ should be connected to the carbonyl C-9′ of a carboxylic acid group. Thus, a structural fragment containing a phenylpropanoid skeleton (Fig. 2, **2F**) was established in compound **1**. Furthermore, HMBC correlations between H-7′ and C-12a/C-13/C-14 and between H-8′ and C-8/C-8a suggested that the two fragments (**1 F** and **2 F**) were connected by C-7′–C-13 and C-8′–C-8 to form a rare ring skeleton (Cavé et al. 1980; Chang et al. 2015; Santos et al. 2019; Yin et al. 2020). Therefore, the plain

Fig. 2 Key HMBC and ^{1}H–^{1}H COSY correlations of compounds **1** and **2**
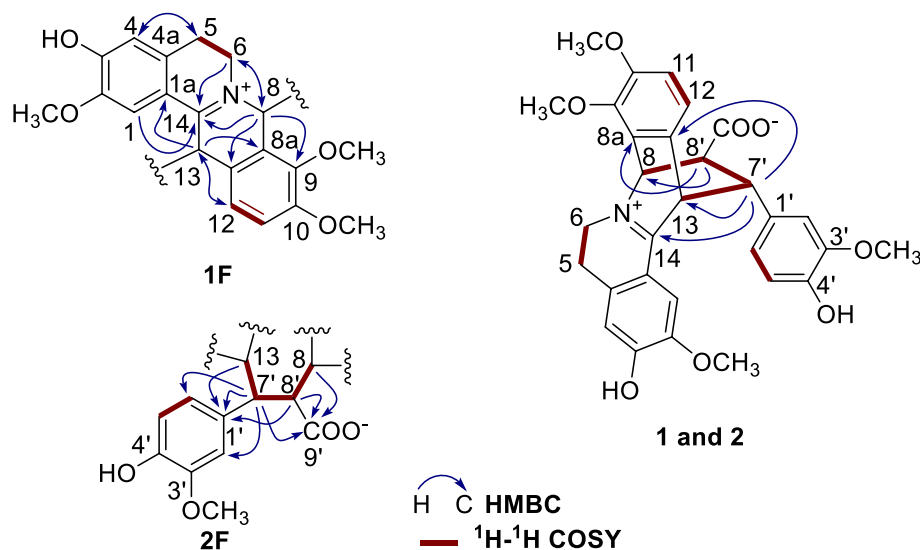
architectural structure of **1** was established to be a zwitteri-onic phenylpropanoid-conjugated protoberberine alkaloid.

The NOESY spectrum of **1** revealed NOE correlations between H-8′ and H-2′/H-6′, indicating that the ABX coupling pattern at C-7′ and the carboxylic acid group at C-8′ remained in the opposite directions. The NOE correlations between H-6a and H-2′/H-6′ suggested that the ABX spin system existed towards the isoquinoline moiety, and the carboxylic acid group occurred facing the AB coupling system (Figs. 3, S19). Thus, the relative configuration of the ABX coupling pattern at C-7′ was 7′α, and that of the carboxylic acid group at C-8′ was determined to be 8′β. The relative configurations of C-8 and C-13 in **1** could not be determined because the NOE correlations of H-8/H-7′ and those of H-13/H-8′ were absent. This may be because both H-8 and H-13 coexist on the plain surface of C-8-C-8′-C-7′-C13, which was supported by the actual 3D structure of **1** in Fig. 4. Fortunately, a crystal that was appropriate for crystallographic analysis was generated

with a mixed solvent of methanol-water (5:1). The X-ray crystallographic analysis revealed that the relative configuration of **1** was a zwitterion, and an ORTEP diagram of **1** is shown in Fig. 4. The optical rotation of **1** is near zero, and no Cotton effect was observed in the ECD spectrum of **1**. Moreover, no flack parameter was found from the crystallographic analysis of **1**, indicating that **1** is a racemic mixture. Chiral resolution of **1** was performed by chiral HPLC separation (Figs. S36, S37, S38) to afford the anticipated enantiomers of (-)-**1** and (+)-**1**, which produced the same NMR data, opposite optical rotations between (−)-**1** ([α]$^{20}_D$ -110.4) and (+)-**1** ([α]$^{20}_D$ +118.1), and mirror image-like ECD curves (Fig. 5). According to the crystallographic analysis of **1**, the ECD curves of the two enantiomers (8*R*,13*S*,7′*R*,8′*S*-**1** and 8*S*,13*R*,7′*S*,8′*R*-**1**) were calculated using the TDDFT theory method for the absolute configuration of (−)-**1** and (+)-**1** (Zhu et al. 2014; Liu et al. 2019). A comparison between the theoretically calculated data and those of the experiment could

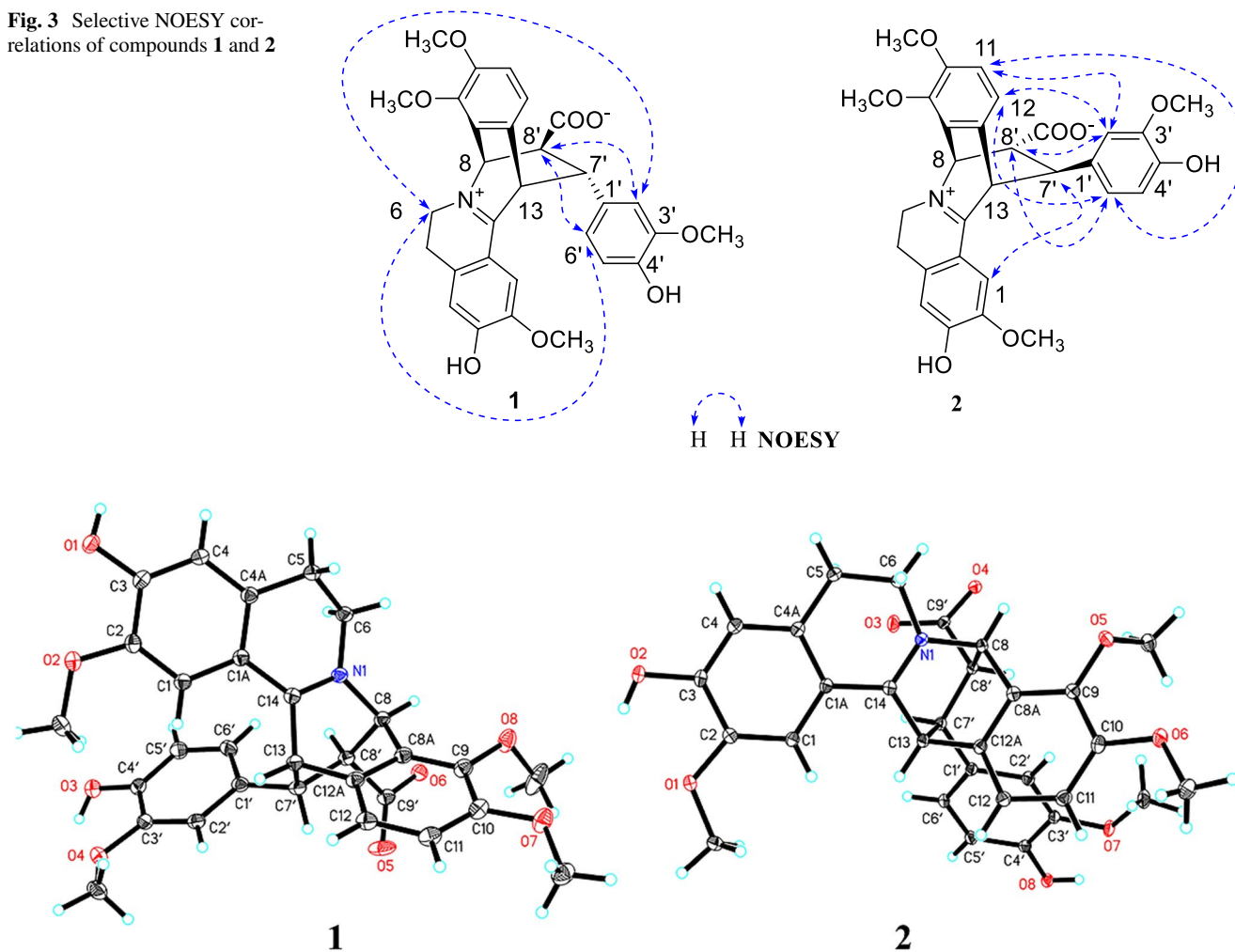**Fig. 3** Selective NOESY correlations of compounds **1** and **2**

Fig. 4 ORTEP diagrams of compounds **1** and **2**
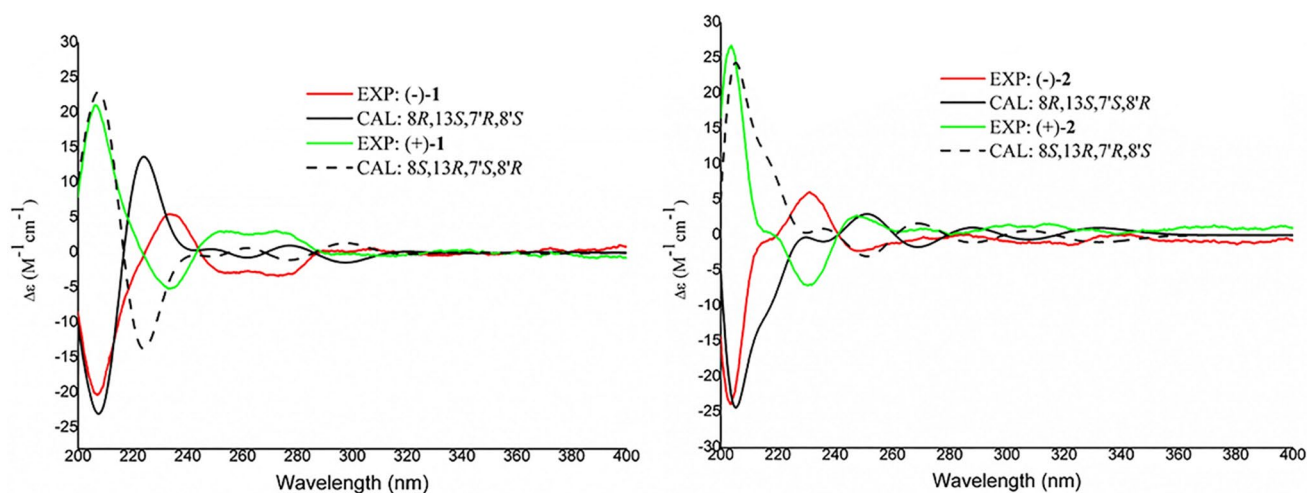
Fig. 5 Experimental and theoretical ECD spectra of compounds (−)-**1** and (+)-**1** and (−)-**2** and (+)-**2**

assign the absolute configurations of (−)-**1** and (+)-**1** as 8*R*,13*S*,7′*R*,8′*S* and 8*S*,13*R*,7′*S*,8′*R*, respectively.

Luckily, the (−)-**1** and (+)-**1** enantiomers offered suitable crystals for crystallographic analysis under the same solvent system of methanol-water (5:1). The absolute stereochemical structures of (−)-**1** and (+)-**1** were further demonstrated by X-ray crystallographic analyses with corresponding flack parameters of 0.03(9) and 0.08(7), respectively. The ORTEP diagrams of (−)-**1** and (+)-**1** are shown in Fig. 6.

(±)-*Epi*-decumicorine A (**2**) was obtained as a light-yellow crystal (absolute EtOH/H$_2$O, 30:1, v/v; m.p. 187–188 °C). The same molecular formula of that for compound **1** (C$_{30}$H$_{29}$NO$_8$) was observed by HR-ESI-TOF-MS analysis (*m/z* 532.1979 [M+H]$^+$, calcd 532.1966). The ^{1}H

and ^{13}C NMR data of **2** (Table 1) are similar to those of **1** with minor variations, in which the chemical shift difference of H-1/H-2′/H-8′ in the ^{1}H NMR spectra is more than 0.5 ppm between **1** and **2**, and those of C-3/C-8a/C-12/C-12a/C-7′/C-9′ in the ^{13}C NMR spectra are larger than 2 ppm between them. In addition, a slight difference in the coupling constant of H-8 was observed between **1** (δ_H 6.00, d, *J* = 3.6) and **2** (δ_H 6.03, d, *J* = 1.2). After 2D NMR (^{1}H–^{1}H COSY, HSQC, and HMBC) analysis, the plain structure of **2** was found to be the same as that of **1**. The small differences in the ^{1}H and ^{13}C NMR data indicated that the chiral carbons of C-8/C-13/C-7′/C-8′ were different between **1** and **2**. Thus, compound **2** was named (±)-*epi*-decumicorine A. Likewise, according to the NOE correlations from H-11 to H-2′/H-6′,
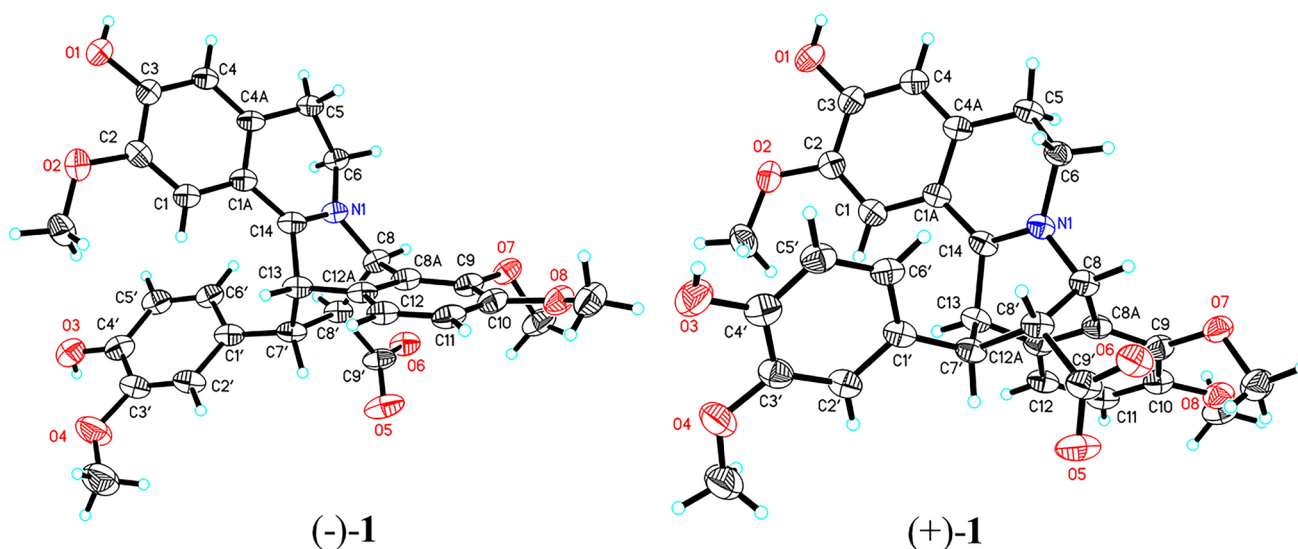

Fig. 6 ORTEP diagrams of compounds (−)-**1** and (+)-**1**

H-12 to H-2′/H-6′, H-8′ to H-2′/H-6′, and H-1 to H-7′ in **2** (Figs. 3, S35), the relative configuration of the ABX spin system at C-7′ occurred as 7′β, and those of the carboxylic acid group at C-8′ existed as 8′α. The single crystal of **2** was produced under a mixed solvent of absolute ethanol-water (30 : 1), and the ORTEP diagram of **2** is shown in Fig. 4, which exhibited opposite chiral carbons with C-7′ and C-8′ than those of **1**. Similarly, compound **2** is also a racemic mixture, which was subjected to chiral HPLC (Figs. S40, S41, S42) separation to afford the two enantiomers of (−)-**2** ([α]$^{20}_D$ − 139.1) and (+)-**2** ([α]$^{20}_D$ + 148.4), and these enantiomers exhibit the same NMR data and mirror image-like ECD curves (Fig. 5). Similar to compound **1**, the absolute configurations of (−)-**2** and (+)-**2** were confirmed to be 8R,13S,7′S,8′R and 8S,13R,7′R,8′S, respectively.

Biomimetic synthesis

A plausible biosynthetic pathway for (±)-**1** and (±)-**2** is shown in Fig. 7. First, based on dopamine and *p*-hydroxy-phenylacetaldehyde derived from the precursor l-tyrosine (Weber and Opatz 2019), the key intermediate (*S*)-reticuline could be produced from a Mannich reaction and subsequent oxidation and methylation reactions (Grycova et al. 2007). Second, transformations from (*S*)-reticuline to berberine were conducted with several enzymes, including berberine

bridge enzyme (BBE), methyltransferase, and (*S*)-tetrahy-droprotoberberine oxidase (STOX) (Grycova et al. 2007). Third, berberine could be converted to jatrorrhizine by reo-pening its methylenedioxy group (Beecher and Kelleher 1983; Rueffer et al. 1983). In addition, *p*-coumaric acid, which is also derived from the precursor l-tyrosine *via* tyrosine ammonia-lyase (TAL), could be transformed to ferulic acid through oxidation, hydrogen transfer with nicotina-mide adenine dinucleotide phosphate (NADPH), and trans-methylation *via* *S*-adenosyl-l-methionine (SAM) (Zhao and Moghadasian 2008). Finally, compounds (±)-**1** and (±)-**2** were generated from a Diels-Alder [4 + 2] cycloaddition reaction between the intermediates of jatrorrhizine and feru-lic acid (Cavé et al. 1980; Chang et al. 2015; Santos et al. 2019; Yin et al. 2020), which is critical for the occurrence of (±)-**1** and (±)-**2**. Based on our improved method (Gupta and Franck 1987), a one-step reaction for the biomimetic synthesis of racemates (±)-**1** and (±)-**2** was developed using jatrorrhizine and ferulic acid as starting materials (Fig. 8). The ratio of (±)-**1** versus (±)-**2** was 1:3, and the isolated yield was 78.3%, as shown in Table 2.

Anti-SARS-CoV-2 activity evaluation

Compounds (-)-**1**, (+)-**1**, (-)-**2**, and (+)-**2** were evalu-ated for their antiviral activity against viral entry into
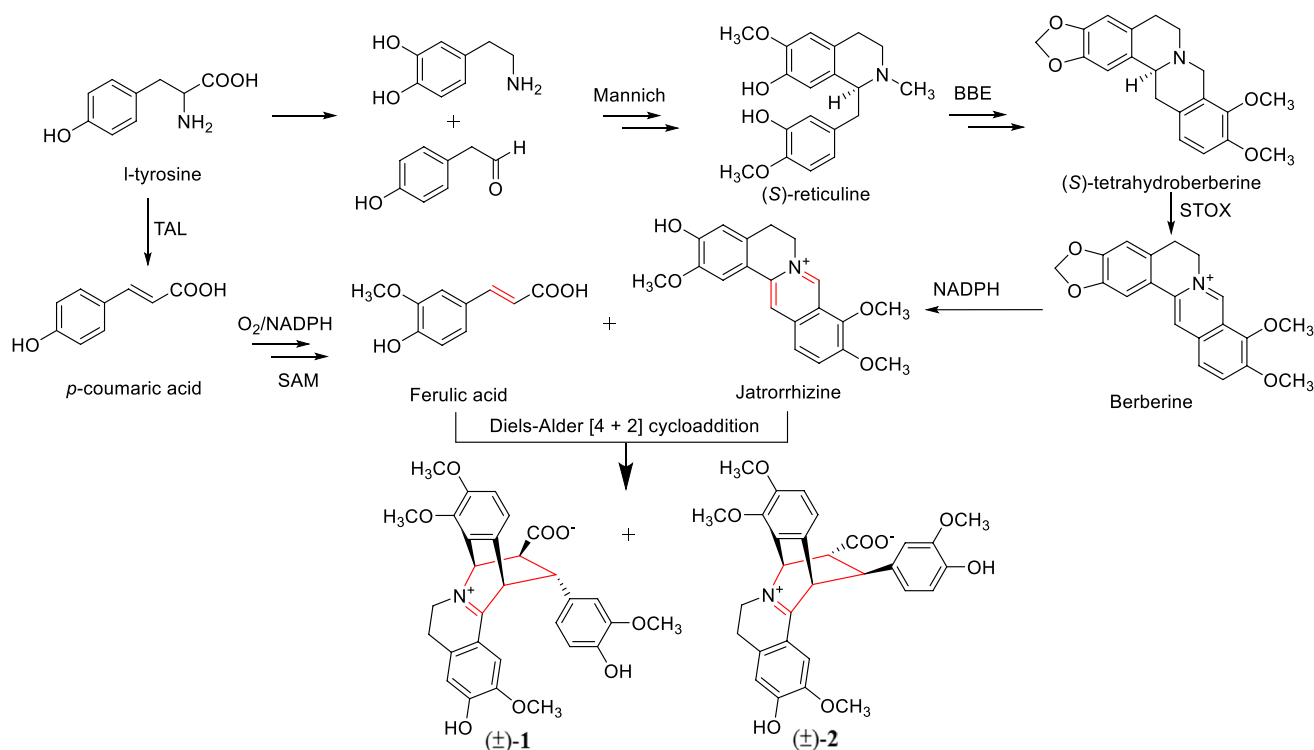

Fig. 7 Proposed biosynthetic pathways for compounds (±)-**1** and (±)-**2**. *BBE* berberine bridge enzyme, *STOX* (*S*)-tetrahydroprotoberberine oxi-dase, *TAL* tyrosine ammonia-lyase, *NADPH* nicotinamide adenine dinucleotide phosphate, *SAM* *S*-adenosyl-l-methionine

HEK-293T-ACE2[h] cells by a SARS-CoV-2 pseudovirus inhibition assay (Guo et al. 2021; Zhang et al. 2021) within their maximum nontoxic concentration of 100 μM. Both SARS-CoV-2 antibody ($IC_{50} = 0.031$ μM) and a reported Evans blue inhibitor ($IC_{50} = 26.95$ μM) (Bojadzic et al. 2021) were employed as positive controls. As a potential anti-SARS-CoV-2 component derived from traditional Chinese medicines (TCMs), glycyrrhizic acid was also examined for its antiviral entry activity in this assay (Yu et al. 2021). Anti-SARS-CoV-2 activity screening was performed with compounds (−)-**1**, (+)-**1**, (−)-**2**, and (+)-**2**, and the results are summarized in Table 3; Fig. 9.

Discussion

Currently, only four Diels-Alder [4 + 2] protoberberine cycloadducts have been discovered from *C. decumbens* (Chang et al. 2015; Yin et al. 2020), *Duguetia staudtii* (Cavé et al. 1980)d *furfuracea* (Santos et al. 2019), in which heterodienes (jatrorrhizine, 5,6-dehydrocoptisine, and 5,6-dehydro-13-methylcoptisine) and dienophiles (fumaric acid, 5-(hydroxymethyl)-2(3H)-furanone, and 2,4,5-trimethoxystyrene) are involved. In contrast to staudine from *D. staudtii* and *D. furfuracea*, compounds **1** and **2** contained one additional carboxylic acid group at C-8′ and

Fig. 8 Biomimetic synthesis of compounds (±)-**1** and (±)-**2**

Table 3 Inhibitory activities of compounds (-)-**1**, (+)-**1**, (-)-**2**, and (+)-**2** against SARS-CoV-2 pseudotyped virus's entry into the HEK-293T-ACE2[h] cells

Compounds	Inhibition rate (%)		
	25 μM	50 μM	100 μM
(−)-**1**	-3.92 ± 8.25	7 ± 5.93	17.23 ± 6.22
(+)-**1**	17.06 ± 6.30	19.89 ± 7.24	28.19 ± 3.61
(−)-**2**	-17.20 ± 3.63	1.02 ± 7.47	23.76 ± 6.54
(+)-**2**	13.02 ± 2.06	10.83 ± 8.27	17.71 ± 2.83
Glycyrrhizic acid	-16.85 ± 9.88	4.01 ± 7.03	11.23 ± 6.96
Evans blue	IC_{50} value of 26.95 ± 4.34 μM		
Antibody inhibitor	IC_{50} value of 0.031 ± 0.003 μM		

Fig. 9 The inhibitory activities of compounds (−)-**1**, (+)-**1**, (−)-**2**, and (+)-**2** against the entry of SARS-CoV-2 pseudovirus into the host cell of HEK-293T-ACE2[h] highly expressing ACE2 receptor. Both antibody ($IC_{50} = 0.031$ μM) and Evans blue ($IC_{50} = 26.95$ μM) inhibitors were used as positive controls in this assay. Glycyrrhizic acid was also examined as an antiviral entry component from TCMs. $*p < 0.05$; $**p < 0.01$; $***p < 0.001$; $****p < 0.0001$ compared with the group of pseudovirus control
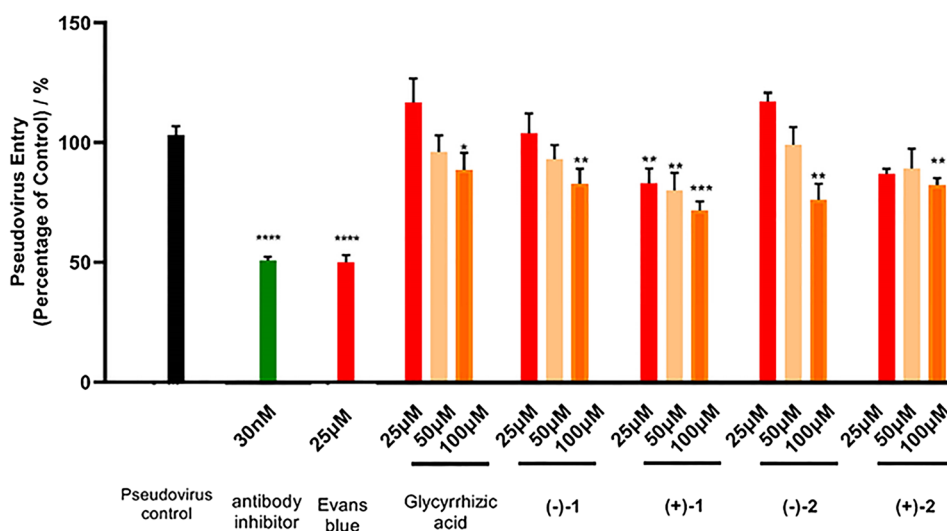
a 4-hydroxy-3-methoxyphenyl group instead of a 2,4,5-trimethoxyphenyl moiety at C-7′, increasing the number of chiral carbons in compounds **1** and **2**. Therefore, ferulic acid was found to be conjugated with protoberberine alkaloid to form zwitterionic [4+2] cycloadducts for the first time.

Based on the biomimetic synthesis of compounds (±)-**1** and (±)-**2** (Fig. 8), Diels-Alder [4+2] cycloaddition occurs under ferulic acid (dienophile in red) and jatrorrhizine (heterodiene in red) to form a tricyclic system that contained four chiral centres and an iminium ion, and this reaction is also known as the inverse-electron-demand Diels-Alder reaction (Wang 2010; Wu and Devaraj 2016). The reaction (Fig. 8) should occur *via* a concerted but nonsynchronous cycloaddition that utilizes a weak charge-transfer complex along the reaction pathway (Bradsher et al. 1979). Theoretically, four racemic compounds could be formed via two types of connections (C-8/C-8′, C-13/C-7′, and C-8/C-7′, C-13/C-8′) in the Diels-Alder reaction of jatrorrhizine and ferulic acid. However, merely two racemates, **1** and **2** with C-8/C-8′ and C-13/C-7′ connections, were discovered in DCR, which was verified by a biomimetic synthesis, suggesting that electronic and steric effects might occur for their paired selectivity (Brocksom et al. 2001). Compounds **1** and **2** should not be artefacts during the isolation process because the compounds were directly detected by LC–MS analysis with the methanol extract of DCR without heating (sonicate for 30 minutes at room temperature) (Fig. S44), and they were not produced via the reaction of jatrorrhizine and ferulic acid in the other four experimental conditions presented in Table 2. Jatrorrhizine is among the main constituents in DCR (Mao et al. 2017). Ferulic acid was also detected in the methanol extract from the crude drug (Fig. S45). As shown in Fig. S44, the amount of compound **2** is more dominant than that of compound **1** in the crude DCR, which is consistent with the biomimetic synthesis result. These results may because less steric effects occur in **2** than

in **1** between the ABX spin system at C-7′ and the isoquinoline group.

Based on the results of the bioactivity screening (Table 3; Fig. 9), compound (+)-**1** reduced the pseudovirus's entry ratio from 17.06 to 28.19% under the tested concentrations (25, 50, 100 μM) in a dose-dependent manner. Under the treatment of 100 μM, compounds (−)-**1**, (−)-**2**, and (+)-**2** also showed antiviral entry activity with inhibitory rates of 17.23%, 23.76%, and 17.71%, respectively. The antiviral entry activities of the four alkaloids were more potent than that of glycyrrhizic acid (inhibition rate of 11.23% at 100 μM). The binding interaction of compound (+)-**1** with the receptor binding domain (RBD) of the viral spike protein was subsequently determined by a biolayer interferometry (BLI) binding assay with human ACE2 protein as a positive control (K_D = 19.39 nM). Compound (+)-**1** bound to the SARS-CoV-2 spike RBD protein with a K_D value of 22.2 μM (Fig. 10). A molecular docking study further confirmed that compound (+)-**1** could bind well to the spike RBD with a calculated interaction energy of −31.8204 kcal/mol (Fig. 11). This indicated that compound (+)-**1** exhibited a specific stereochemical structure-activity relationship for targeting the spike protein to perform antiviral entry activity against SARS-CoV-2.

In this study, phenylpropanoid-conjugated protoberberine alkaloids were shown to suppress SARS-CoV-2 viral entry by targeting the spike RBD. During the SARS-CoV-2 pandemic, targeting the SARS-CoV-2 spike was considered a safe and promising strategy for the research and development of anti-SARS-CoV-2 reagents/drugs. The phenylpropanoid-conjugated protoberberines could be a new type of chemical with antiviral effects by targeting spike protein, which might be helpful for the rational design and synthesis of more potent antiviral molecules that target spike protein.

In summary, we reported two pairs of enantiomeric isoquinoline alkaloids that possess a novel carbon skeleton
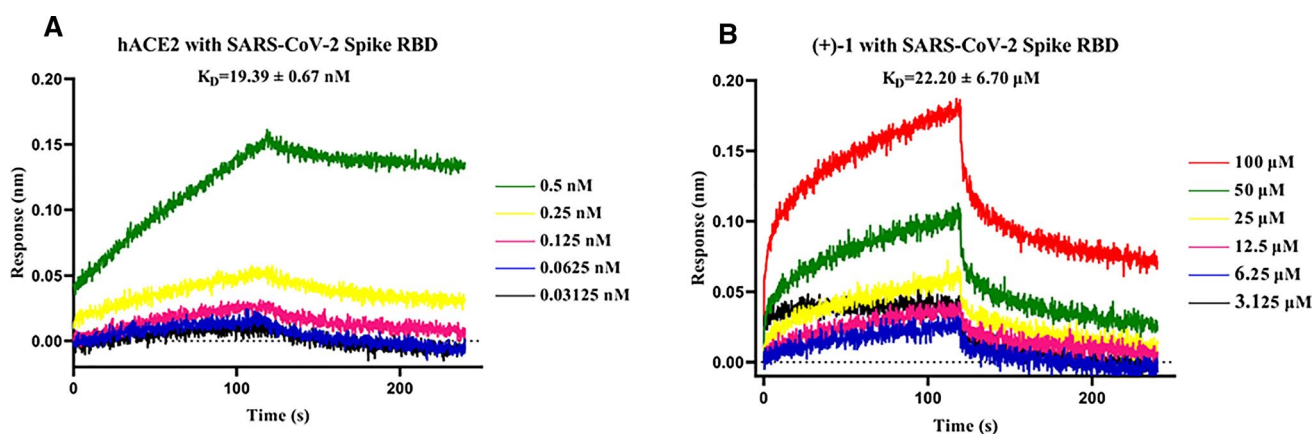

Fig. 10 Dose-response curves of **A** human ACE2 protein and **B** compound (+)-**1** binding to SARS-CoV-2 spike RBD protein. The concentrations were 0.03125~0.5 nM for human ACE2 protein, and 3.12~100 μM for Compound (+)-**1**, respectively
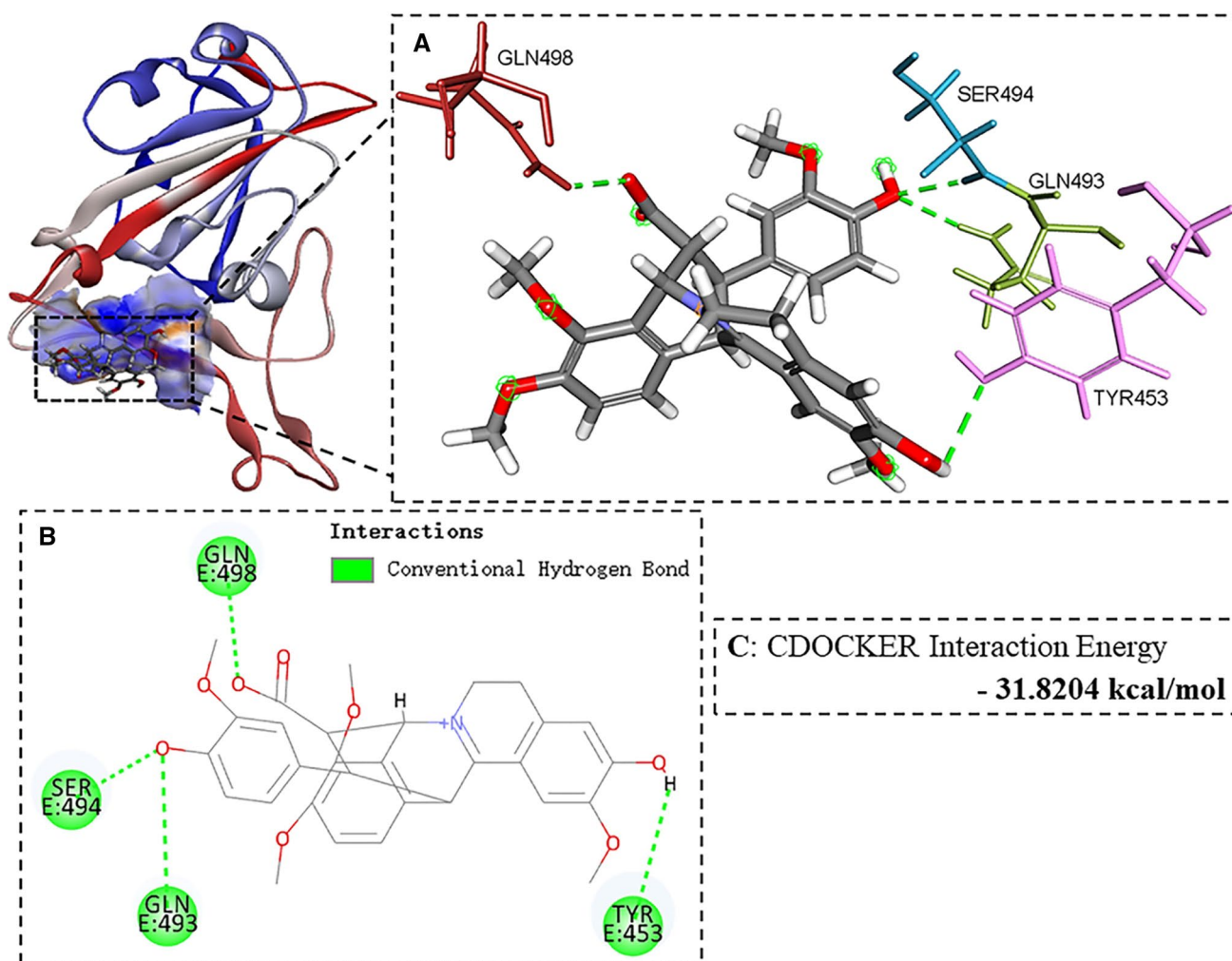
Fig. 11 Docking simulation of compound (+)-**1** in the active sites of SARS-CoV-2 spike RBD protein (PDB code: 6M0J). **A** 3D interaction model of (+)-**1** with spike RBD protein. **B** 2D interaction model of (+)-**1** with spike RBD protein. **C** CDOCKER interaction energy of (+)-**1** with spike RBD protein. The result revealed that compound (+)-**1** interacts with the amino residues of GLN493, GLN498, TYR453, and SER494 in spike RBD protein with a calculated CDOCKER interaction energy of −31.8204 kcal/mol

of phenylpropanoid-conjugated protoberberine from the rhizomes of *C. decumbens*. The absolute configurations of compounds (−)-**1**, (+)-**1**, (−)-**2**, and (+)-**2** were determined by NMR, ECD calculations and X-ray crystallographic analyses. The biomimetic syntheses of (±)-decumicorine A and (±)-*epi*-decumicorine A were validated by a one-step Diels-Alder [4 + 2] cycloaddition reaction. Compound (+)-**1** demonstrated potential anti-SARS-CoV-2 activity by preventing viral spikes from attaching to the ACE2 receptor on host cells.

Declarations

References

Beecher CWW, Kelleher WJ (1983) The incorporation of berberine into jatrorrhizine. Tetrahedron Lett 24:469–472. https://doi.org/10.1016/S0040-4039(00)81439-2

Bojadzic D, Alcazar O, Chen J, Chuang ST, Condor Capcha JM, Shehadeh LA, Buchwald P (2021) Small-molecule inhibitors of the

coronavirus spike: ACE2 protein-protein interaction as blockers of viral attachment and entry for SARS-CoV-2. ACS Infect Dis 7:1519–1534. https://doi.org/10.1021/acsinfecdis.1c00070

Bradsher CK, Day FH (1971) Cycloaddition of ethylene derivatives with isoquinolinium salts. Tetrahedron Lett 12:409–410. https://doi.org/10.1016/S0040-4039(01)96453-6

Bradsher CK, Carlson GLB, Adams MG (1979) Cationic polar cycloaddition of cyclopropenes. J Org Chem 44:1199–1202. https://doi.org/10.1021/jo01322a002

Brocksom TJ, Nakamura J, Ferreira ML, Brocksom U (2001) The Diels-Alder reaction: an update. J Braz Chem Soc 12:597–622. https://doi.org/10.1590/s0103-50532001000500004

Cavé A, Kunesch N, Leboeuf M, Bévalot F, Chiaroni A, Riche C (1980) Alcaloïdes Des Annonacées XXV: La Staudine, Nouvel Alcaloïde Isoquinoléique du Pachypodanthium staudtii Engl. et Diels. J Nat Prod 43:103–111. https://doi.org/10.1021/np50007a008

Chang J, Chu Z-B, Song J, Jin L, Sun X (2015) Two novel isoquinoline alkaloids from the seedling of Corydalis decumbens. Tetrahedron Lett 56:225–228. https://doi.org/10.1016/j.tetlet.2014.11.077

Deng AP, Zhang Y, Zhou L, Kang CZ, Lv CG, Kang LP, Nan TG, Zhan ZL, Guo LP, Huang LQ (2021) Systematic review of the alkaloid constituents in several important medicinal plants of the genus Corydalis. Phytochemistry 183:112644. https://doi.org/10.1016/j.phytochem.2020.112644

Ding X, Wu Y, Wang Y, Vilseck JZ, Brooks CL 3 (2020) Accelerated CDOCKER with GPUs, parallel simulated annealing, and fast fourier transforms. J Chem Theory Comput 16:3910–3919. https://doi.org/10.1021/acs.jctc.0c00145

Dolomanov OV, Bourhis LJ, Gildea RJ, Howard JaK, Puschmann H (2009) OLEX2: a complete structure solution, refinement and analysis program. J Appl Crystallogr 42:339–341. https://doi.org/10.1107/S0021889808042726

Grycova L, Dostal J, Marek R (2007) Quaternary protoberberine alkaloids. Phytochemistry 68:150–175. https://doi.org/10.1016/j.phytochem.2006.10.004

Guo Y, Meng JR, Liu JZ, Xu T, Zheng ZY, Jiang ZH, Bai LP (2021) Synthesis and biological evaluation of honokiol derivatives bearing 3-((5-phenyl-1,3,4-oxadiazol-2-yl)methyl)oxazol-2(3H)-ones as potential viral entry inhibitors against SARS-CoV-2. Pharmaceuticals (Basel) 14:885. https://doi.org/10.3390/ph14090885

Gupta RB, Franck RW (1987) Cycloadditions of isoquinolinium salts: evidence for a two-step mechanism in a stereocontrolled synthesis of substituted tetralins. J Am Chem Soc 109:5393–5403. https://doi.org/10.1021/ja00252a015

Iranshahy M, Quinn RJ, Iranshahi M (2014) Biologically active isoquinoline alkaloids with drug-like properties from the genus Corydalis. RSC Adv 4:15900–15913. https://doi.org/10.1039/c3ra47944g

Kratzert D, Holstein JJ, Krossing I (2015) DSR: enhanced modelling and refinement of disordered structures with SHELXL. J Appl Crystallogr 48:933–938. https://doi.org/10.1107/S1600576715005580

Liu X, Yang J, Fu J, Yao X-J, Wang J-R, Liu L, Jiang Z-H, Zhu G-Y (2019) Aggreganoids A–F, carbon-bridged sesquiterpenoid dimers and trimers from Lindera aggregata. Org Lett 21:5753–5756. https://doi.org/10.1021/acs.orglett.9b02166

Mallamo JP, Earley WG, Kumar V, Subramanyam C, Dority JA Jr, Miller MS, Dehaven-Hudkins DL, Ault B, Herrmann JL Jr, Dung JS et al (1994) Identification, synthesis, and characterization of a unique class of N-methyl-D-aspartate antagonists. The 6,11-ethanobenzo[b]quinolizinium cation. J Med Chem 37:4438–4448. https://doi.org/10.1021/jm00052a003

Mao Z, Di X, Zhang J, Wang X, Liu Y, Di X (2017) Rapid and cost-effective method for the simultaneous quantification of seven alkaloids in Corydalis decumbens by microwave-assisted extraction and capillary electrophoresis. J Sep Sci 40:3008–3014. https://doi.org/10.1002/jssc.201700051

Neese F (2012) The ORCA program system. WIREs Comput Mol Sci 2:73–78. https://doi.org/10.1002/wcms.81

Neese F (2018) Software update: the ORCA program system, version 4.0. WIREs Comput Mol Sci 8:e1327. https://doi.org/10.1002/wcms.1327

Rueffer M, Ekundayo O, Nagakura N, Zenk MH (1983) Biosynthesis of the protoberberine alkaloid jatrorrhizine. Tetrahedron Lett 24:2643–2644. https://doi.org/10.1016/S0040-4039(00)87966-6

Santos TCB, De Oliveira RC, De Vasconcelos LG, Sousa PTD, Silva VCP, De Carvalho MG, Ribeiro TaN (2019) Chemical constituents from roots of Duguetia furfuracea (A. St.-Hil.) Saff. (Annonaceae). Biochem Syst Ecol 87:103951. https://doi.org/10.1016/j.bse.2019.103951

Shang J, Ye G, Shi K, Wan Y, Luo C, Aihara H, Geng Q, Auerbach A, Li F (2020) Structural basis of receptor recognition by SARS-CoV-2. Nature 581:221–224. https://doi.org/10.1038/s41586-020-2179-y

Stephens PJ, Harada N (2010) ECD cotton effect approximated by the Gaussian curve and other methods. Chirality 22:229–233. https://doi.org/10.1002/chir.20733

Tantillo DJ (2021) Drawing polycyclic molecules. ACS Omega 6:23008–23014. https://doi.org/10.1021/acsomega.1c03607

Wang Z (2010) Bradsher cycloaddition. In: Wang Z (ed) Comprehensive organic name reactions and reagents, 1st edn. Wiley, New Jersey, pp 506–510. https://doi.org/10.1002/9780470638859.conrr112

Weber C, Opatz T (2019) Bisbenzylisoquinoline alkaloids. Alkaloids Chem Biol 81:1–114. https://doi.org/10.1016/bs.alkal.2018.07.001

Wu H, Devaraj NK (2016) Inverse electron-demand Diels-Alder bioorthogonal reactions. Top Curr Chem (Cham) 374:3. https://doi.org/10.1007/s41061-015-0005-z

Yin X, Jia H, Zhang Q, Jiang Y, Tu P (2020) (+)- and (-)-Corydecumbenines A and B, two pairs of novel quaternary protoberberine alkaloid cycloadduct enantiomers with anti-neuroinflammatory and neuroprotective activities from the rhizomes of Corydalis decumbens. Bioorg Chem 104:104251. https://doi.org/10.1016/j.bioorg.2020.104251

Yu S, Zhu Y, Xu J, Yao G, Zhang P, Wang M, Zhao Y, Lin G, Chen H, Chen L, Zhang J (2021) Glycyrrhizic acid exerts inhibitory activity against the spike protein of SARS-CoV-2. Phytomedicine 85:153364. https://doi.org/10.1016/j.phymed.2020.153364

Zhang Y, Hu S, Wang J, Xue Z, Wang C, Wang N (2021) Dexamethasone inhibits SARS-CoV-2 spike pseudotyped virus viropexis by binding to ACE2. Virology 554:83–88. https://doi.org/10.1016/j.virol.2020.12.001

Zhao Z, Moghadasian MH (2008) Chemistry, natural sources, dietary intake and pharmacokinetic properties of ferulic acid: a review. Food Chem 109:691–702. https://doi.org/10.1016/j.foodchem.2008.02.039

Zhu G-Y, Yao X-J, Liu L, Bai L-P, Jiang Z-H (2014) Alistonitrine A, a caged monoterpene indole alkaloid from Alstonia scholaris. Org Lett 16:1080–1083. https://doi.org/10.1021/ol403625g